FRONTIERS OF PHYSICS

RESEARCH ARTICLE
Volume 21 / Issue 6 / 062203 / 2026

# Optomagnomechanical mass sensor enhanced by higher-order exceptional point

Ming-Song Ding[1,†], Feng-Yang Zhang[2,‡]

1 Department of Basic Education, Dalian Polytechnic University, Dalian 116034, China
2 School of Physics and Materials Engineering, Dalian Minzu University, Dalian 116600, China
Corresponding authors. E-mail: †dingms@dlpu.edu.cn, ‡dllgzfy@126.com
Received December 11, 2025; accepted April 17, 2026



## ABSTRACT

In non-Hermitian physics, exceptional points (EPs) hold great potential for quantum technologies, while optomagnomechanical (OMM) systems offer a versatile platform for exploring such effects. Here, we propose a third-order EP-enhanced OMM mass sensor, where the eigenfrequency evolution of the system is directly mapped to the optical cavity output spectrum. We demonstrate that the third-order EP delivers a strongly enhanced eigenfrequency response to tiny mass perturbations, achieving over two orders of magnitude higher frequency sensitivity than conventional EP-free OMM systems, without requiring strong optomagnomechanical coupling or high-intensity driving. The sensing mechanism relies on mass-induced mechanical frequency shifts that lift the EP degeneracy and split eigenfrequencies, enabling high-sensitivity detection via the linear scaling between the cube of the eigenfrequency shift and target adsorbed mass. Spectral analysis confirms optimal measured spectral resolution (MSR) at the EP under gain-dissipation balance, with the performance enhancement originating from the intrinsic properties of the third-order EP rather than cavity gain. This scheme breaks the sensitivity bottleneck of traditional OMM sensors, paving the way for ultrasensitive nanoparticle detection and quantum metrology.

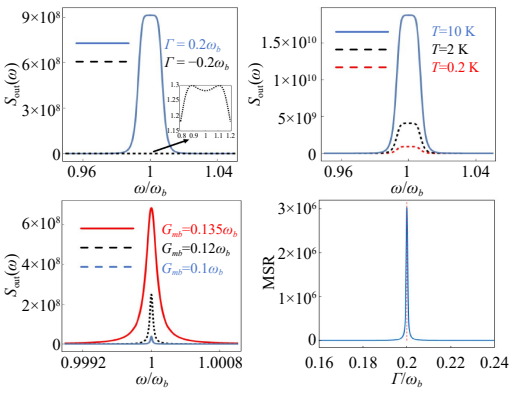


**Keywords** optomagnomechanical system, higher-order exceptional point, mass sensor

## 1 Introduction

Optomagnomechanical (OMM) systems have emerged as a promising platform in quantum information science and metrology, attracting extensive attention from both theoretical and experimental research communities [1–6]. In these hybrid systems, the photon–phonon coupling is realized via radiation pressure interaction, while the magnon–phonon coupling is mediated by the magnetostrictive effect in ferrimagnetic materials such as yttrium iron garnet (YIG). Benefiting from a series of intrinsic advantages including the high magnetic-field tunability of the magnon mode, ultra-low magnon damping in YIG, and coherent multi-degree-of-freedom coupling between photons, magnons and phonons. OMM systems have enabled a series of important research advances, including optical sensing of magnons [7], magnon-to-optics quantum state transfer [8], microwave-optics entanglement generation [9], high-efficiency entanglement generation of microwave fields [10], magnonic squeezed states [11], and robust entanglement distribution protocols [12, 13].


https://doi.org/10.15302/frontphys.2026.062203

In parallel, non-Hermitian physics has opened a new paradigm for breaking the sensitivity limit of traditional precision sensors, centered around the concept of exceptional points (EPs) – spectral singularities arising from the full coalescence of eigenvalues and eigenvectors in non-Hermitian systems [14–21]. EP-based sensing leverages the enhanced nonlinear response of eigenfrequencies to external perturbations, overcoming the fundamental sensitivity limits of conventional linear optical mass detection [22–24]. Traditional mass sensors based on mechanical oscillators follow a linear mass-frequency scaling relation [25], which inherently constrains the upper limit of sensitivity. In contrast, EP-based sensors enable a nonlinear power-law scaling between the frequency response and perturbation strength, as widely demonstrated in various second-order EP-based coupled-cavity systems [26–32]. Notably, such second-order EP sensors have achieved an order-of-magnitude enhancement in mass sensitivity over conventional EP-free designs [30], without the need for external signal amplification circuits.

Beyond conventional second-order EPs, non-Hermitian systems host a rich hierarchy of higher-order EPs, defined as spectral singularities where three or more eigenmodes fully coalesce. Higher-order EPs offer significant performance advantages over second-order counterparts, particularly for ultra-sensitive sensing [33–36], spontaneous emission enhancement [37], and topological photonics [38, 39]. Recent theoretical and experimental advances in photonic and optomechanical platforms have demonstrated that higher-order EPs enable orders-of-magnitude improvements in sensor sensitivity, owing to their stronger power-law response to tiny perturbations [27, 34, 40–45]. While higher-order EPs have been extensively explored in photonic and electronic platforms, their potential in OMM mass sensing remains underexploited. This research gap motivates the development of OMM-based mass sensors exploiting higher-order EPs.

Meanwhile, OMM systems face inherent limitations for high-sensitivity mass sensing, primarily due to the weak bare magnomechanical coupling strength ($< 1$ Hz in most platforms [46]), which fundamentally limits measurement sensitivity. To overcome this intrinsic sensitivity bottleneck, we integrate a third-order EP with the optomagnomechanical mass sensor. Unlike most reported EP-enhanced sensors confined to photonic, electronic or pure optomechanical platforms [30, 33], our OMM-based design provides a new route to overcome the fundamental sensitivity limit of conventional OMM sensors: it uses the third-order EP to markedly amplify the intrinsically weak bare magnomechanical coupling, and achieves significant sensitivity enhancement directly based on this amplified coupling. The magnon mode's active magnetic-field tunability enables precise and flexible control of third-order EP conditions, a unique advantage not available in conventional all-optical EP sensing platforms. We further clarify that the enhancement of our scheme originates from the intrinsic properties of the third-order EP, rather than cavity gain alone, resolving the ambiguity over the origin of performance enhancement in EP-based sensors.

We establish a third-order EP in the non-Hermitian OMM system, by introducing a gain-assisted cavity mode and tuning the driving strengths of the magnon and optical modes. In our scheme, the adsorption of an ultratiny target mass on the mechanical resonator induces a minute mechanical frequency shift, which lifts the third-order EP degeneracy and splits the three eigenfrequencies of the system, a response directly mapped to the optical cavity output spectrum. By selecting the well-resolved eigenfrequency shift as the sensing signal, we establish a correlation between the eigenfrequency response and the target adsorbed mass, leveraging the cube-root scaling of the third-order EP to weak perturbations. We also investigate the output spectral characteristics of the system, as well as the impacts of thermal noise on EP working stability and the measured spectral resolution (MSR), to verify the practical feasibility of our sensing scheme.

This work is structured as follows: Section 2 formulates the physical model and dynamical equations of the investigated OMM system; Section 3 derives the quantitative relationship between adsorbed mass and eigenfrequency shift at the third-order EP; Section 4 quantifies and compares the eigenfrequency response enhancement factor of the proposed non-Hermitian system against conventional EP-free OMM configurations; Section 5 analyzes the optical cavity output spectrum and investigates the impacts of the third-order EP and thermal noise on the system's spectral characteristics; finally, Section 6 summarizes the key findings of this work and discusses their relevant implications.

## 2 Model and dynamical equations

We consider an OMM system, which consists of three modes: a magnon mode, a mechanical phonon mode, and a cavity photon mode. In this system, collective spin excitations are induced by placing a YIG sphere in a uniform bias magnetic field and driving the sphere with a microwave field, thereby generating magnons. Mechanical phonons are supported by the YIG structure, whose excellent mechanical properties enable its surface to act as a high-quality mechanical resonator. Surface phonons in YIG spheres are coupled to magnons via magnetostrictive interaction. Photons in an external optical cavity are coupled to the mechanical vibrations of the YIG sphere, which are enhanced by a high-reflectivity mirror pad [47]. Due to the significantly lower frequencies of the phonons compared to the magnons and cavity photons, both nonlinear couplings can be treated as

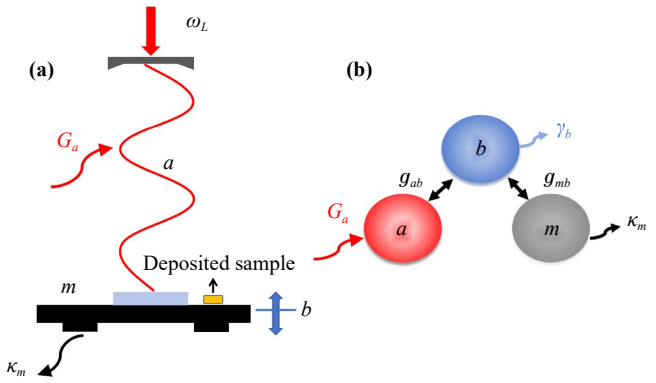


**Fig. 1** **(a)** Schematic of the OMM system wherein mechanical displacement couples concurrently to the magnon mode via dispersive magnetostrictive interaction and to the optical mode through radiation pressure. **(b)** The equivalent mode-coupling model.

dispersive interactions of the radiation pressure.

The YIG sphere can be replaced by a micro-bridge YIG crystal [9, 47, 48], as illustrated in Fig. 1(a). In this configuration, the cavity photon mode $a$ can be implemented by attaching a microscale, high-reflectivity mirror pad [gray mirror on the black microbridge in Fig. 1(a)] to the surface of the YIG microbridge. Given the superior material properties of YIG, the microbridge functions as a mechanical resonator supporting the vibrational mode $b$. For mass sensing applications, the mirror pad must be fabricated with sufficiently small dimensions and minimal mass to preserve the mechanical quality factor and oscillation characteristics. Furthermore, the deformation displacement perpendicular to the attachment surface is approximately uniform (with negligible bending displacement), enabling the YIG micro-bridge and mirror pad to co-vibrate as an integrated structure at nearly identical frequencies. In our sensing scheme, the target analyte is deposited on the YIG micro-bridge, and its mass is quantified by detecting the induced eigenfrequency shift of the OMM system.

As shown in the equivalent mode-coupling model in Fig. 1(b), the system consists of an active optical cavity mode $a$, a passive magnon mode $m$, and a mechanical mode $b$. The active cavity $a$ can be made from $Er^{3+}$-doped silica [49]. The cavity mode $a$ is driven by a pump laser field with frequency $\omega_L$ and intensity $E_a$, while the magnon mode $m$ is driven by a microwave magnetic field with frequency $\omega_M$ and intensity $E_m$. In a rotating frame defined by the pump frequencies $\omega_M$ and $\omega_L$, the total Hamiltonian of this OMM system ($\hbar = 1$) is given by

$$\begin{aligned} H_{\rm tot} = {} & \Delta_m m^\dagger m + \Delta_a a^\dagger a + \omega_b b^\dagger b + g_{mb} m^\dagger m (b^\dagger + b) \\ & + g_{ab} a^\dagger a (b^\dagger + b) + {\rm i}E_a (a^\dagger + a) + {\rm i}E_m (m^\dagger + m), \end{aligned} \tag{1}$$

where $\Delta_{m(a)} = \omega_{m(a)} - \omega_{M(L)}$ is the detuning between the frequency of the magnon (photon) mode $\omega_{m(a)}$ and $\omega_{M(L)}$. The frequency $\omega_m$ can be tuned by an external bias magnetic field $H$, expressed as $\omega_m = \gamma_g H$, where $\gamma_g/(2\pi) = 28$ GHz/T represents the gyromagnetic ratio of YIG [50]. The annihilation (creation) operators $m(m^\dagger)$, $a(a^\dagger)$ and $b(b^\dagger)$ correspond to the magnon, photon, and phonon modes, respectively. $\omega_b$ represents the resonance frequency of the mechanical mode. $g_{mb}$ and $g_{ab}$ denote the magnon-phonon and photon-phonon coupling rates, respectively. Besides, the pump intensities for the cavity and magnon modes are given by $E_a = \sqrt{\kappa_a P_L/\omega_L}$ and $E_m = \frac{\sqrt{5}}{4}\gamma_g\sqrt{N}B_0$ [7], where $\kappa_a$ is the cavity decay rate, $P_L$ corresponds to the laser power, $N$ indicates the total number of spins, and $B_0$ is the amplitude of the microwave magnetic field.

By incorporating the corresponding damping and noise terms for each mode, the evolution of the OMM system is described by the following Heisenberg–Langevin equations:

$$\begin{aligned} \dot{m} = {} & -({\rm i}\Delta_m + \kappa_m)m - {\rm i}g_{mb}m(b^\dagger + b) + E_m + \sqrt{2\kappa_m}m_{\rm in}, \\ \dot{a} = {} & -({\rm i}\Delta_a - \Gamma)a - {\rm i}g_{ab}a(b^\dagger + b) + E_a + \sqrt{2\kappa_a}a_{\rm in}, \\ \dot{b} = {} & -({\rm i}\omega_b + \gamma_b)b - {\rm i}g_{mb}m^\dagger m - {\rm i}g_{ab}a^\dagger a + \sqrt{2\gamma_b}b_{\rm in}, \end{aligned} \tag{2}$$

where $\Gamma = -\kappa_a + G_a$ denotes an effective cavity gain with gain rate $G_a$. $\kappa_m$ and $\gamma_b$ represent loss rates of the magnon and phonon modes, respectively. The input vacuum noise operator $o_{in}$ ($o = m,\ a,\ b$) corresponds to zero expectation value, i.e., $\langle o_{in}\rangle = 0$. The non-zero correlation functions are $\langle o_{in}^\dagger(t)o_{in}(t')\rangle = N_o(\omega_o)\delta(t-t')$ and $\langle o_{in}(t)o_{in}^\dagger(t')\rangle = [N_o(\omega_o)+1]\delta(t-t')$, where $N_o(\omega_o) = [\exp(\hbar\omega_o/(k_B T)) - 1]^{-1}$ and $T$ are the equilibrium mean thermal excitation number per mode and the bath temperature, respectively. Here, the Markovian approximation has been taken, which is valid for a large mechanical quality factor $Q_m = \omega_b/\gamma_b \gg 1$ [1].

Under continuous driving, the system evolves to a steady state. When the amplitudes of the magnon mode and the cavity mode are sufficiently large, $|\langle m\rangle|$, $|\langle a\rangle| \gg 1$, we decompose each mode operator as the sum of its classical steady-state average and a quantum fluctuation operator, i.e., $o = o_s + \delta o$ ($o = m,\ a,\ b$), and neglect the small second-order fluctuation terms. Consequently, Eq. (2) is separated into two sets of linear equations: one for the classical steady-state averages and one for the quantum fluctuations. Solving the set of equations for the classical averages, we have

$$\begin{aligned} m_s &= \frac{E_m}{{\rm i}\tilde{\Delta}_m + \kappa_m}, \\ a_s &= \frac{E_a}{{\rm i}\tilde{\Delta}_a - \Gamma}, \\ b_s &= \frac{-{\rm i}g_{mb}|m_s|^2 - {\rm i}g_{ab}|a_s|^2}{{\rm i}\omega_b + \gamma_b}, \end{aligned} \tag{3}$$

where $\tilde{\Delta}_m = \Delta_m + g_{mb}(b_s + b_s^*)$ and $\tilde{\Delta}_a = \Delta_a + g_{ab}(b_s + b_s^*)$ are the effective detunings of the magnon mode and cavity mode, respectively. This model builds upon a critical feature of standard OMM systems: condition $g_{mb}, g_{ab} \ll \Delta_{m(a)}, \omega_b$ is typically satisfied [7]. And the condition enables the equality $\tilde{\Delta}_{m(a)} \simeq \Delta_{m(a)}$, thereby simplifying Eq. (3) and yielding its corresponding steady-state solution.

By applying the aforementioned transformations $o = o_s + \delta o$ to Eq. (2), we obtain the dynamical equations for the quantum fluctuation operators

$$\begin{aligned}
\delta\dot{m} =& -(\mathrm{i}\tilde{\Delta}_m + \kappa_m)\delta m - \mathrm{i}G_{mb}(\delta b + \delta b^\dagger) + \sqrt{2\kappa_m}m_{\mathrm{in}},\\
\delta\dot{a} =& -(\mathrm{i}\tilde{\Delta}_a - \Gamma)\delta a - \mathrm{i}G_{ab}(\delta b + \delta b^\dagger) + \sqrt{2\kappa_a}a_{\mathrm{in}},\\
\delta\dot{b} =& -(\mathrm{i}\omega_b + \gamma_b)\delta b - \mathrm{i}(G_{mb}^*\delta m + G_{ab}^*\delta a + \mathrm{h.c.})\\
&+ \sqrt{2\gamma_b}b_{\mathrm{in}},
\end{aligned} \tag{4}$$

where $G_{mb} = g_{mb}m_s$ and $G_{ab} = g_{ab}a_s$ are the effective coupling strengths, and they can be tuned by changing $E_m$ and $E_a$. For simplicity, we assume $G_{mb} = |G_{mb}|$ and $G_{ab} = |G_{ab}|$ hereafter. For mass sensing measurements, the tiny adsorbed mass only shifts the mechanical resonance frequency, and does not alter the bare coupling coefficients $g_{mb}$ and $g_{ab}$. The effective couplings $G_{mb}$ and $G_{ab}$ are governed by the steady-state mode amplitudes and driving parameters, which also remain unchanged under the weak mass perturbation in this work. By rewriting the equations of motion in Eq. (4) as $\delta\dot{m} = -\mathrm{i}[\delta m, H_{\mathrm{eff}}] + \sqrt{2\kappa_m}m_{\mathrm{in}}$, $\delta\dot{a} = -\mathrm{i}[\delta a, H_{\mathrm{eff}}] + \sqrt{2\kappa_a}a_{\mathrm{in}}$ and $\delta\dot{b} = -\mathrm{i}[\delta b, H_{\mathrm{eff}}] + \sqrt{2\gamma_b}b_{\mathrm{in}}$, we obtain the linearized effective Hamiltonian (including dissipative terms) as

$$\begin{aligned}
H_{\mathrm{eff}} =& \omega_{m,\mathrm{eff}}\delta m^\dagger\delta m + \omega_{a,\mathrm{eff}}\delta a^\dagger\delta a + \omega_{b,\mathrm{eff}}\delta b^\dagger\delta b\\
&+ (G_{mb}\delta m^\dagger + G_{ab}\delta a^\dagger + h.c.)(\delta b + \delta b^\dagger),
\end{aligned} \tag{5}$$

where $\omega_{m,\mathrm{eff}} = \tilde{\Delta}_m - \mathrm{i}\kappa_m, \omega_{a,\mathrm{eff}} = \tilde{\Delta}_a + \mathrm{i}\Gamma$ and $\omega_{b,\mathrm{eff}} = \omega_b - \mathrm{i}\gamma_b$. We then consider the magnon and cavity modes to be red-detuned with identical driving frequencies $\tilde{\Delta}_m = \tilde{\Delta}_a = \omega_b$. Under this condition, we apply the rotating-wave approximation (RWA) and neglect the rapidly oscillating terms $(G_{mb}\delta m^\dagger + G_{ab}\delta a^\dagger)\delta b^\dagger$ and $(G_{mb}^*\delta m + G_{ab}^*\delta a)\delta b$ in Eq. (5). Consequently, the linearized effective Hamiltonian $H_{\mathrm{eff}}$ simplifies to the following matrix representation:

$$H_{\mathrm{eff}} = \begin{pmatrix} \omega_{m,\mathrm{eff}} & 0 & G_{mb} \\ 0 & \omega_{a,\mathrm{eff}} & G_{ab} \\ G_{mb}^* & G_{ab}^* & \omega_{b,\mathrm{eff}} \end{pmatrix}. \tag{6}$$

For Eq. (6), when condition $|H_{\mathrm{eff}} - \Omega I| = |H_{\mathrm{eff}}^* - \Omega I| = 0$ is satisfied, where $I$ is an identity matrix and $\Omega$ is the eigenvalue of the Hamiltonian $H_{\mathrm{eff}}$, the system is parity-time ($\mathcal{PT}$) symmetric [41]. This condition is mathematically described by the following set of equations:

$$\begin{aligned}
\kappa_m G_{mb}^2 - \Gamma G_{ab}^2 + \Gamma\kappa_m\gamma_b = 0,\\
\Gamma - \kappa_m - \gamma_b = 0,\\
G_{ab}^2 + G_{mb}^2 - \kappa_m\Gamma - \gamma_b(\Gamma + \kappa_m) = 0.
\end{aligned} \tag{7}$$

From the preceding equations, the effective coupling strengths at the EP are obtained as

$$\begin{aligned}
G_{mb,\mathrm{EP}} &= \sqrt{\kappa_m^3/(\kappa_m + \Gamma)},\\
G_{ab,\mathrm{EP}} &= \sqrt{\Gamma^3/(\kappa_m + \Gamma)}.
\end{aligned} \tag{8}$$

Equation (8) gives the unique analytical solution to the $\mathcal{PT}$ -symmetry and triple-degeneracy constraints in Eq. (7). This set of coupling strengths provides the sufficient and necessary condition for the system to reach the third-order EP, only when $G_{mb}$ and $G_{ab}$ take the values in Eq. (8) can all three eigenvalues and eigenvectors of the effective Hamiltonian fully coalesce, realizing the third-order spectral degeneracy required for our enhanced sensing scheme.

The following experimentally achievable parameters are given [7, 51–55]: $\omega_b/(2\pi) = 10$ MHz, $\gamma_b = 10^{-5}\omega_b$, $g_{mb}/(2\pi) = 0.2$ Hz and $g_{ab}/(2\pi) = 100$ Hz. The gain of the cavity mode $\Gamma = 0.2\omega_b$, and the decay rate of magnon mode $\kappa_m = \Gamma - \gamma_b$. Due to $\gamma_b \ll \Gamma, \kappa_m$, Eq. (8) can be approximated as $G_{mb,\mathrm{EP}} \simeq G_{ab,\mathrm{EP}} \simeq \sqrt{\kappa_m\Gamma/2}$ in the subsequent discussion. The real and imaginary parts of the eigenvalues of the effective Hamiltonian $H_{\mathrm{eff}}$ as a function of the coupling $G_{mb}$ are plotted in Fig. 2. It can be seen that when $G_{mb} > G_{mb,\mathrm{EP}}$, the eigenfrequencies of the system are real and non-degenerate, confirming the system resides in the $\mathcal{PT}$-symmetry phase (PTSP). Conversely, for $G_{mb} < G_{mb,\mathrm{EP}}$, the system enters the $\mathcal{PT}$-symmetry-broken phase (PTBP), characterized by complex eigenfrequencies. The EP, where the phase transition occurs, is precisely located at $G_{mb} = G_{mb,\mathrm{EP}}$, marking the boundary between these two regimes. Here, $G_{mb,\mathrm{EP}}/(2\pi) \simeq 1.4$ MHz implies $B_0 \simeq 4.8 \times 10^{-6}$ T, which corresponds to a microwave drive power of approximately 3.5 mW [50]. Owing to the high parametric sensitivity of third-order EPs, active stabilization of the microwave drive power is required to maintain this precise power level and hold the system stably at the target EP condition. This is readily achieved with commercial microwave sources offering sub-μW power stability, confirming the practical viability of our scheme.

## 3 Mass sensor at the exceptional point

The fundamental mechanism of mass sensing in conventional mechanical oscillator systems relies on monitoring the mechanical frequency shift ($\varepsilon$) induced by adsorbed mass ($\delta m$) on the surface of the resonator, and the quantitative relationship between $\delta m$ and $\varepsilon$ is given by [25]

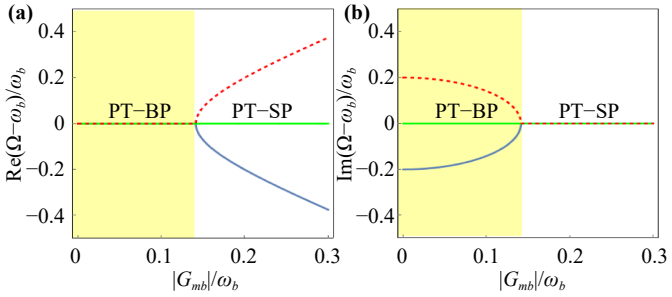


**Fig. 2** **(a)** and **(b)** show the real and imaginary parts of the eigenfrequencies of the effective Hamiltonian versus the coupling strengths $G_{mb}$. And three lines of different colors represent three eigenfrequencies, respectively. Light yellow and white patches are used to label $\mathcal{PT}$-symmetry-breaking phase (PTBP) and $\mathcal{PT}$-symmetry phase (PTSP). The figures are obtained for $G_{mb} = G_{ab}$. The other parameters used are listed in the main text.

$$\delta m \simeq \frac{2m}{\omega_b}\varepsilon, \tag{9}$$

where $m$ is the mass of the mechanical resonator. From this equation, it is evident that for a conventional mechanical oscillator system without EPs, the frequency shift scales linearly with the adsorbed mass, which fundamentally limits the maximum achievable sensitivity.

We now detail the sensing advantages of the third-order EP in our OMM system, and demonstrate its performance enhancement over conventional mechanical frequency-shift sensing schemes. When the coupling strengths satisfy Eq. (8), the adsorption of a target analyte on the mechanical resonator induces a shift in the mechanical resonance frequency. This perturbation modifies the system's eigenfrequencies, which are governed by the effective Hamiltonian $H_{\mathrm{eff}}$ and satisfy the characteristic equation:

$$(\Omega-\omega_b)^3 + \varepsilon(\Omega-\omega_b)^2 - \mathrm{i}\gamma_b\varepsilon(\Omega-\omega_b) + \kappa_m\Gamma\varepsilon = 0. \tag{10}$$

Following the nondimensionalization of the above equation ($\Omega' = (\Omega-\omega_b)/\omega_b$ and $\tilde{\varepsilon} = \varepsilon/\omega_b$), we have $\Omega'^3 + \tilde{\varepsilon}\Omega'^2 - \mathrm{i}\gamma_b\tilde{\varepsilon}\Omega'/\omega_b + \kappa_m\Gamma\tilde{\varepsilon}/\omega_b^2 = 0$. As shown in Fig. 3(a), the mechanical frequency shift induced by adsorbed mass lifts the EP degeneracy, thus inducing a split and shift of the system's eigenfrequencies. Among the three eigenfrequency shifts, one is negative while the other two are positive. Figure 3(b) displays the linewidth variation of the eigenfrequencies, where the difference between the maximum linewidth and minimum linewidth progressively increases with increasing mechanical frequency shift.

The eigenfrequencies shown in Figs. 3(a) and (b) are not abstract, unobservable theoretical quantities, but rather physical quantities directly mapped to the output

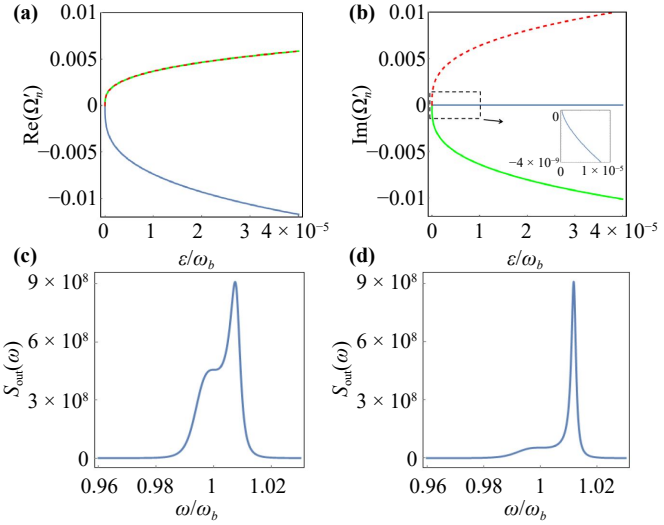


**Fig. 3** **(a)** The eigenfrequency shifts versus the mechanical frequency shift $\varepsilon$ induced by adsorbed mass. **(b)** The linewidth of the eigenfrequency versus the mechanical frequency shift $\varepsilon$. **(c)** Output spectrum of the OMM system at $\varepsilon/\omega_b = 10^{-5}$. **(d)** Output spectrum of the OMM system at $\varepsilon/\omega_b = 4\times10^{-5}$, panels (c) and (d) are obtained at $T = 0.2$ K. And all other parameters are consistent with those used in Fig. 2.

spectra. Specifically, the real parts of the eigenfrequencies correspond directly to the central frequencies of the output spectra, while the imaginary parts correspond directly to their linewidths. Here, we leverage the output spectra derived in the subsequent section V to demonstrate the scenario during actual measurements. Figure 3(c) shows that when the mechanical frequency shift induced by the adsorbed mass reaches $\varepsilon/\omega_b = 10^{-5}$, the spectrum splits: the lower spectral peaks on the left correspond to the eigenfrequencies represented by the green and red solid lines in Fig. 3(a), while the higher peak on the right corresponds to the eigenfrequency represented by the blue solid line in Fig. 3(a). Figure 3(d) illustrates that as the mechanical frequency shift further increases to $\varepsilon/\omega_b = 4\times10^{-5}$, the spectral splitting becomes more pronounced, with the narrower peak on the right corresponding to the eigenfrequency represented by the blue solid line in Fig. 3(b). In practical spectral measurements, the peak corresponding to the blue solid line is chosen as the main target for the sensor.

This selection is based on two critical criteria: First, the real parts of the other two eigenfrequencies are nearly degenerate, making them indistinguishable in experimental spectral measurements. In contrast, the eigenfrequency shift represented by the blue solid line shows a significant deviation from the other two and exhibits a higher peak intensity, which facilitates its detection. Second, the linewidth (imaginary part of the eigenfrequency) is orders of magnitude smaller than the magnitude of the eigenfrequency shift (real part), which

is fundamentally advantageous for enhancing measurement resolution. To clearly illustrate the dependence of the eigenfrequency on the perturbation $\tilde{\varepsilon}$, we expand the dimensionless form of Eq. (10) using the Newton-Puiseux series. Given $\tilde{\varepsilon} \ll 1$, only the first two terms are retained in the expansion, i.e., $\Omega' = c_1\tilde{\varepsilon}^{\frac{1}{3}} + c_2\tilde{\varepsilon}^{\frac{2}{3}}$, where $c_1$ and $c_2$ are constants. Substituting this truncated series into the equation referenced above yields three solution sets for $c_1$ and $c_2$:

$$\begin{aligned}
\Omega_1' &= -(\kappa_m\Gamma/\omega_b^2)^{1/3}\tilde{\varepsilon}^{1/3} - \frac{1}{3}\mathrm{i}\gamma_b(\omega_b\kappa_m\Gamma)^{-1/3}\tilde{\varepsilon}^{2/3},\\
\Omega_2' &= (\kappa_m\Gamma/\omega_b^2)^{1/3}\mathrm{e}^{-\mathrm{i}\pi/3}\tilde{\varepsilon}^{1/3} + \frac{1}{3}\mathrm{i}\gamma_b(\omega_b\kappa_m\Gamma)^{-1/3}\mathrm{e}^{\mathrm{i}\pi/3}\tilde{\varepsilon}^{2/3},\\
\Omega_3' &= (\kappa_m\Gamma/\omega_b^2)^{1/3}\mathrm{e}^{\mathrm{i}\pi/3}\tilde{\varepsilon}^{1/3} + \frac{1}{3}\mathrm{i}\gamma_b(\omega_b\kappa_m\Gamma)^{-1/3}\mathrm{e}^{-\mathrm{i}\pi/3}\tilde{\varepsilon}^{2/3}.
\end{aligned} \tag{11}$$

In Eq. (11), $\Omega_1'$ denotes the blue solid line in Fig. 3, where its real part corresponds to the eigenfrequency shift, and its imaginary part to the linewidth of the corresponding eigenmode. A narrower linewidth implies that the mass sensor possesses a higher measurement resolution. Numerically, based on the (nondimensionalizing) eigenfrequency shift $\delta\varepsilon = -\mathrm{Re}(\Omega_1') = (\kappa_m\Gamma/\omega_b^2)^{1/3}\tilde{\varepsilon}^{1/3}$, the mass calculation formula originally denoted as Eq. (9) is redefined as

$$\delta m = \frac{2m\omega_b^2}{\kappa_m\Gamma}(\delta\varepsilon)^3. \tag{12}$$

## 4 Sensitivity at the exceptional point

The key parameters governing mass resolution are the eigenfrequency shift and linewidth of the eigenmode in this system. As demonstrated by the blue solid line in Figs. 3(a) and (b), the eigenfrequency shift (real part of $\Omega_1'$) exceeds the linewidth (imaginary part of $\Omega_1'$) by several orders of magnitude, allowing us to neglect the contribution of the linewidth and focus solely on the eigenfrequency shift. To quantify the mass-sensing sensitivity at the EP, the sensor sensitivity $\left|\mathrm{Re}(\Delta\Omega^{\mathrm{EP}})\right|$ is defined as the real part $\Omega_1'\omega_b$[56], with its expression given by:

$$\left|\mathrm{Re}(\Delta\Omega^{\mathrm{EP}})\right| = \left|\mathrm{Re}(\Omega_1'\omega_b)\right| = \sqrt[3]{\omega_b\kappa_m\Gamma}\,\tilde{\varepsilon}^{1/3}. \tag{13}$$

Figure 4(a) plots the nonlinear dependence of the sensor sensitivity on the mechanical frequency shift, with the logarithmic inset confirming the expected cube-root scaling of sensitivity with perturbation strength.

Conventional passive optomagnomechanical mass sensors rely on the linear relationship between adsorbed mass $\delta m$ and mechanical frequency shift $\varepsilon$ for mass sensing. In contrast, our proposed scheme leverages the nonlinear scaling between the eigenfrequency shift at the third-order EP and the adsorbed mass, achieving significantly enhanced sensing sensitivity. To quantitatively characterize this sensitivity enhancement, a dimensionless eigenfrequency response enhancement factor $\eta$ for mass sensing is defined as

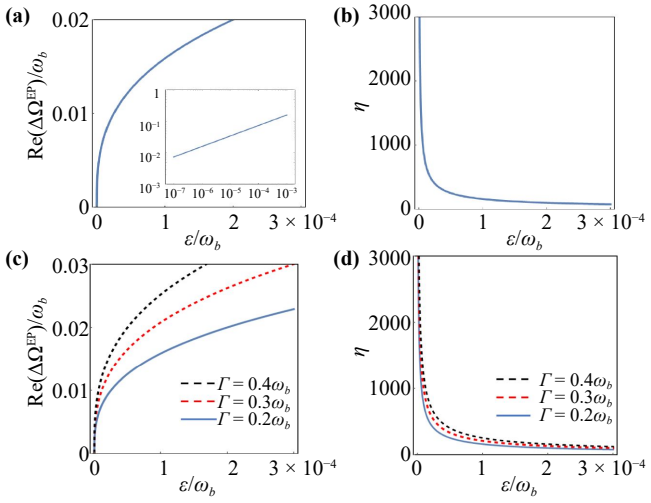


**Fig. 4** **(a)** The sensor sensitivity versus the mechanical frequency shift $\varepsilon$ induced by adsorbed mass. The inset employs logarithmic axes to better illustrate the data. **(b)** The eigenfrequency response enhancement factor $\eta$ versus the mechanical frequency shift $\varepsilon$. **(c)** The sensor sensitivity versus the mechanical frequency shift $\varepsilon$ at different decay(gain) rates. **(d)** The eigenfrequency response enhancement factor $\eta$ versus the mechanical frequency shift $\varepsilon$ at different decay(gain) rates. Here, $\kappa_m = \Gamma - \gamma_b$, and all other parameters are consistent with those used in Fig. 2.

$$\eta = \left|\frac{\mathrm{Re}(\Delta\Omega^{\mathrm{EP}})}{\varepsilon}\right| = \sqrt[3]{4m^2\kappa_m\Gamma/(\omega_b^2\delta m^2)}. \tag{14}$$

As demonstrated in Fig. 4(b), at a perturbation of $\varepsilon/\omega_b = 2\times10^{-4}$ (a physically observable range), the eigenfrequency response enhancement factor $\eta$ reaches approximately 100 ($\delta m/m \simeq 4\times10^{-6}$), corresponding to a 100-fold sensitivity improvement over conventional EP-free OMM systems. Notably, $\eta$ decreases as the mechanical frequency shift $\varepsilon$ increases, approaching unity in the limit of large perturbations. Conversely, smaller mass perturbations yield larger sensitivity enhancements within the valid range of our perturbative expansion, where the eigenfrequency shift remains larger than the spectral linewidth, confirming the inverse scaling between perturbation strength and EP-enhanced sensing performance.

Figure 4(c) shows the sensor sensitivity as a function of the mechanical frequency shift for different gain (decay) rates. The results confirm that higher gain and dissipation rates yield higher sensitivity for a fixed mechanical perturbation. Figure 4(d) plots the dependence of the eigenfrequency response enhancement factor $\eta$ for

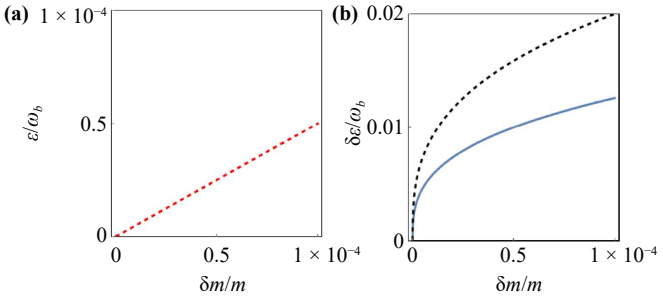


**Fig. 5** **(a)** The mechanical frequency shift for a conventional sensing scheme versus the adsorbed mass. **(b)** The eigenfrequency shift (at the EP) versus the adsorbed mass at different gain(decay) rates. The blue solid curve corresponds to $\Gamma/(2\pi) = 2$ MHz, whereas the black dashed curve represents the case for $\Gamma/(2\pi) = 4$ MHz. $\kappa_m = \Gamma - \gamma_b$, and all other parameters are consistent with those used in Fig. 2.

mass sensing on the mechanical frequency shift for different gain (decay) rates, showing that $\eta$ varies nonlinearly with the gain and dissipation rates. As derived from Eq. (8), higher dissipation and gain rates lead to enhanced optomagnomechanical coupling strengths at the EP, which amplifies the system's response to the perturbation of mechanical mode, ultimately leading to an improvement in sensing sensitivity.

Figure 5 demonstrates the comparative performance of our proposed scheme, where both the eigenfrequency shift $\delta\varepsilon/\omega_b$ at the EP and mechanical frequency shift $\varepsilon/\omega_b$ exhibit clear dependence on the adsorbed mass. Specifically, Fig. 5(a) depicts the mechanical frequency shift $\varepsilon/\omega_b$ generated by conventional mass sensors according to Eq. (9), while the blue solid line in Fig. 5(b) illustrates the eigenfrequency shift $\delta\varepsilon/\omega_b$ achieved by our scheme according to Eq. (12) under identical parameter conditions to those in Fig. 5(a). A direct comparison of the vertical coordinates corresponding to the red dashed line in Fig. 5(a) and the blue solid line in Fig. 5(b) demonstrates the superior performance of the mass sensor based on eigenfrequency shift. Furthermore, Fig. 5(b) quantitatively analyzes the influence of varying gain(decay) rates on the eigenfrequency shift.

## 5 Output spectra at the exceptional point

Quantum and thermal noise fundamentally limit the performance of mass sensors, and EP-enhanced sensing faces a well-known trade-off: while EPs boost the frequency response to mass perturbations, they also amplify noise, which can degrade the overall signal-to-noise ratio (SNR) [57–59]. This trade-off has long been a key bottleneck for EP-based sensors, but recent works have demonstrated noise-resilient EP sensing schemes [60, 61]. with ongoing research exploring methods to mitigate this limitation, including via nonlinear phenomena [62–64].

In this section, we theoretically characterize the output spectrum of the cavity mode, investigate how the EP modifies the system's spectral response, and evaluate the robustness of the sensing scheme against thermal noise.

The dynamical equations for the system's quantum fluctuations can be derived from Eq. (6) as follows:

$$\begin{aligned}
\delta\dot{m} &= -(\mathrm{i}\tilde{\Delta}_m + \kappa_m)\delta m - \mathrm{i}G_{mb}\delta b + \sqrt{2\kappa_m}m_{\mathrm{in}},\\
\delta\dot{a} &= -(\mathrm{i}\tilde{\Delta}_a - \Gamma)\delta a - \mathrm{i}G_{ab}\delta b + \sqrt{2\kappa_a}a_{\mathrm{in}},\\
\delta\dot{b} &= -(\mathrm{i}\omega_b + \gamma_b)\delta b - \mathrm{i}(G^*_{mb}\delta m + G^*_{ab}\delta a) + \sqrt{2\gamma_b}b_{\mathrm{in}}.
\end{aligned} \tag{15}$$

Cavity field fluctuations are far more experimentally accessible to measure in the frequency domain than in the time domain. Hence, employing the Fourier transform definition for an operator $O(\omega) = \int_{-\infty}^{\infty} O(t)\mathrm{e}^{-\mathrm{i}\omega t}\mathrm{d}t$, Eq. (15) can be written in Fourier domain. According to the input–output theory, the relationship between output field, cavity field, and input noise operator is given by the relation $\delta a_{\mathrm{out}}(\omega) = \sqrt{2\kappa_a}\delta a(\omega) - a_{\mathrm{in}}(\omega)$. Then the expressions for the transmitted cavity field in Fourier domain are given by

$$\delta a_{\mathrm{out}}(\omega) = S_1(\omega)a_{\mathrm{in}}(\omega) + S_2(\omega)m_{\mathrm{in}}(\omega) + S_3(\omega)b_{\mathrm{in}}(\omega), \tag{16}$$

where

$$\begin{aligned}
S_1(\omega) &= \frac{2\kappa_a}{K_3(\omega)} - 1,\\
S_2(\omega) &= -\frac{G_{mb}G_{ab}\sqrt{4\kappa_a\kappa_m}}{K_1(\omega)K_2(\omega)K_3(\omega)},\\
S_3(\omega) &= \frac{-\mathrm{i}G_{ab}\sqrt{4\kappa_a\gamma_b}}{K_2(\omega)K_3(\omega)},
\end{aligned} \tag{17}$$

where $K_1(\omega) = -\mathrm{i}\omega + \mathrm{i}\tilde{\Delta}_m + \kappa_m$, $K_2(\omega) = -\mathrm{i}\omega + \mathrm{i}\omega_b + \gamma_b + G^2_{mb}/K_1(\omega)$ and $K_3(\omega) = -\mathrm{i}\omega + \mathrm{i}\tilde{\Delta}_a - \Gamma + G^2_{mb}/K_2(\omega)$. Substituting Eq. (17) into the noise operator correlation functions, we derive the output spectrum, defined as

$$\begin{aligned}
S_{\mathrm{out}}(\omega) &= \int[\langle\delta a^\dagger_{\mathrm{out}}(\omega)\delta a_{\mathrm{out}}(\omega')\rangle + \langle\delta a_{\mathrm{out}}(\omega)\delta a^\dagger_{\mathrm{out}}(\omega')\rangle]\mathrm{d}\omega'\\
&= (2N_a+1)\left|S_1(\omega)\right|^2 + (2N_m+1)\left|S_2(\omega)\right|^2\\
&\quad + (2N_b+1)\left|S_3(\omega)\right|^2.
\end{aligned} \tag{18}$$

Figure 6(a) plots the output spectra for a non-Hermitian OMM system at the EP ($\Gamma = 0.2\omega_b$), characterized by a gain cavity mode, and a standard OMM system with a lossy cavity mode ($\Gamma = -0.2\omega_b$). The superiority of the non-Hermitian system's output spectrum is evident, underscoring its potential for enhanced mass sensor performance. The influence of temperature (thermal

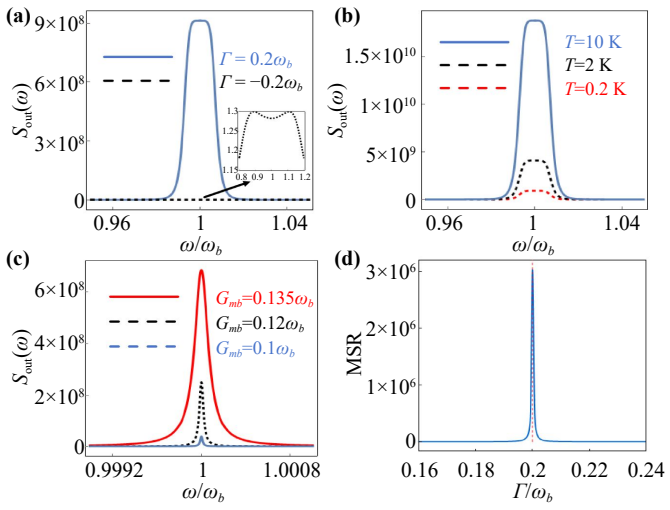


**Fig. 6** **(a)** Output spectra of the non-Hermitian OMM system at the exceptional point (EP, $\Gamma = 0.2\omega_b$, solid line) versus a standard OMS with a lossy cavity mode $\Gamma = -0.2\omega_b$, dashed line), demonstrating enhanced performance under EP conditions. **(b)** Thermal noise effects: signal amplification accompanied by linewidth broadening. **(c)** Spectral evolution during deviation from the EP, revealing intensity reduction and rapid linewidth narrowing. **(d)** MSR versus the gain $\Gamma$. Except for Fig. 6(b), panels (a), (c), and (d) are obtained at $T = 0.2$ K. All other parameters are consistent with those used in Fig. 2.

noise) on the output spectrum is depicted in Fig. 6(b). We find that the EP-induced signal enhancement effect persists under thermal noise. This signal enhancement phenomenon has also been confirmed in Ref. [32]. It is noteworthy that enhanced thermal noise also leads to increased spectral linewidth, implying a concurrent reduction in signal resolution alongside signal amplification. This performance degradation becomes far more severe at room temperature, where drastically amplified thermal noise and sharply reduced mechanical quality factor will completely overwhelm the EP-induced sensitivity enhancement. For our current device architecture, a cryogenic environment is therefore essential to maintain the ultrasensitive mass detection performance demonstrated in this work.

In Fig. 6(c), we demonstrate that considering the effect of ambient temperature and without altering the gain and loss of the system, the peak of the output spectrum decreases as $G_{mb}$ gradually deviates from the value required for the EP, with the linewidth of the output spectrum reducing correspondingly, where $G_{mb,\mathrm{EP}} \simeq 0.14\omega_b$ corresponds to the system operating at the high-order EP. In the measurement of spectral signals, the ratio of spectral intensity to the square root of the linewidth ($\frac{\text{spectral intensity}}{\sqrt{\text{spectral width}}}$) is generally strongly correlated with the MSR [23]. We assume that the above two are equivalent in this system. To explore the relationship

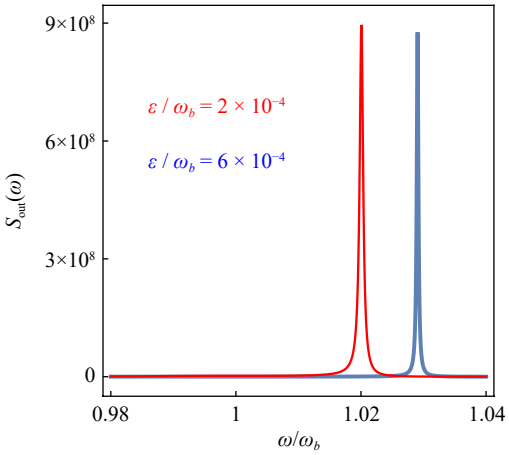


**Fig. 7** Central frequency shift of the output spectra at different mechanical frequency shift $\varepsilon/\omega_b$. The temperature is $T = 0.2$ K, and all other parameters are consistent with those used in Fig. 2.

between the MSR and the gain and loss of the cavity and magnon modes, we plot the dependence of MSR on the gain coefficient of the cavity mode in Fig. 6(d). It can be observed that the MSR of the system reaches its maximum when the cavity gain matches the magnon dissipation, satisfying the EP condition ($\Gamma = \kappa_m = 0.2\omega_b$). This result confirms that the third-order EP significantly improves the measurement resolution, even though thermal noise is also amplified at the EP. In contrast, gain-loss imbalance leads to a sharp drop in MSR, which degrades the measurement accuracy. Furthermore, no MSR enhancement is observed when $\Gamma$ exceeds the EP condition, verifying that the performance improvement of our scheme originates from the intrinsic properties of the third-order EP, rather than the cavity gain alone.

In addition, owing to the high parameter sensitivity of EP systems and the incompleteness of the noise considered in this work, our future research will focus on investigating the SNR at the EP, and exploring whether the introduction of nonlinearity can significantly facilitate a further SNR enhancement in the OMM system.

As shown in Fig. 7, we present the evolution of the output spectra with mechanical frequency shift $\varepsilon/\omega_b$ induced by adsorbed mass at the EP. It can be seen that as $\varepsilon/\omega_b$ increases, the central frequency of the spectral peak gradually shifts away from the resonance frequency at zero adsorbed mass ($\omega/\omega_b = 1$). In practical measurements, the magnitude of the adsorbed mass can be inversely calculated from this frequency shift $\delta\varepsilon$ via Eq. (12). Notably, for the range of $\varepsilon/\omega_b$ values shown in Fig. 7, only the spectral peak corresponding to the eigenfrequency represented by the blue solid line in Fig. 3(b) remains observable among the three peaks associated with the split eigenfrequencies, while the other two peaks are negligible due to their extremely weak intensities.

## 6 Conclusion

In this work, we have theoretically proposed and characterized a third-order EP-enhanced OMM mass sensor, addressing the long-standing sensitivity bottleneck caused by weak intrinsic magnomechanical coupling in conventional OMM systems. We have confirmed that the system's eigenfrequency evolution is directly observable via the optical cavity output spectrum, which serves as the experimental readout port. The real and imaginary parts of the system's eigenfrequencies map to the central frequency and linewidth of the spectral resonance peaks, respectively. The degeneracy and lifting of the third-order EP are reflected in the transition from a single degenerate spectral peak to split, shifted peaks, enabling quantitative mass detection via measurable spectral frequency shifts.

Our scheme has achieved over two orders of magnitude higher frequency sensitivity than conventional EP-free OMM systems, without requiring strong optomagnomechanical coupling or high-intensity driving. We have further verified that the system attains optimal MSR at the EP under strict gain-dissipation balance, with the EP working condition maintainable under practical cryogenic thermal noise, and have confirmed that the performance enhancement originates from the intrinsic properties of the third-order EP rather than cavity gain alone. Overall, this work has demonstrated the feasibility of third-order EP engineering for alleviating the sensitivity bottleneck of conventional OMM mass sensors, and provides a promising route for ultrasensitive nanoparticle detection and quantum metrology.

**Declarations** The authors declare that they have no competing interests and there are no conflicts.

**Data availability** Data underlying the results presented in this paper are not publicly available at this time but may be obtained from the authors upon reasonable request.

**Acknowledgements** The work was supported by the National Natural Science Foundation of China (NSFC) (Grant No. 92565106), Liaoning Provincial Special Funds for Basic Research Operations of Universities (Grant No. LJ212410152021), Liaoning Provincial PhD Research Initiation Fund Program (Grant No. 2024-BS-191), and the Fundamental Research Funds for the Central Universities (Grant No. 04442024074).

## References

1. X. Zuo, Z. Y. Fan, H. Qian, M. S. Ding, H. Tan, H. Xiong, and J. Li, Cavity magnomechanics: from classical to quantum, *New J. Phys.* 26(3), 031201 (2024)
2. A. Sohail, R. Ahmed, J. X. Peng, T. Munir, A. Shahzad, S. K. Singh, and M. C. de Oliveira, Controllable Fano-type optical response and four-wave mixing via magnetoelastic coupling in an opto-magnomechanical system, *J. Appl. Phys.* 133(15) (2023)
3. Y. T. Yan, C. Li, and L. Zhou, Nonreciprocal amplification in an opto-magnomechanical system, *Opt. Express* 33(12), 25146 (2025)
4. J. Cao, M. R. Wei, Q. Guo, H. Tan, G. Li, and T. Zhang, Generation and manipulation of one-way steering in optomagnomechanical system, *Adv. Quantum Technol.* 8(8), 2400547 (2025)
5. C. Zhang, X. Liu, L. Gao, R. Yang, J. Zhang, and T. Zhang, Generation of optomicrowave and optomagnonic entanglements in cascaded opto-magnomechanical systems, *Opt. Express* 33(16), 33330 (2025)
6. Q. Zheng, W. Zhong, G. Cheng, and A. Chen, Nonreciprocal macroscopic tripartite entanglement in atom-opto-magnomechanical system, *EPJ Quantum Technol.* 11(1), 8 (2024)
7. Z. Y. Fan, R. C. Shen, Y. P. Wang, J. Li, and J. Q. You, Optical sensing of magnons via the magnetoelastic displacement, *Phys. Rev. A* 105(3), 033507 (2022)
8. Z. Y. Fan, H. Qian, and J. Li, Stationary optomagnonic entanglement and magnon-to-optics quantum state transfer via opto-magnomechanics, *Quantum Sci. Technol.* 8(1), 015014 (2023)
9. Z. Y. Fan, L. Qiu, S. Gröblacher, and J. Li, Microwave-optics entanglement via cavity optomagnomechanics, *Laser Photonics Rev.* 17(12), 2200866 (2023)
10. K. Di, S. Tan, L. Wang, A. Cheng, X. Wang, Y. Liu, and J. Du, High-efficiency entanglement of microwave fields in cavity opto-magnomechanical systems, *Opt. Express* 31(18), 29491 (2023)
11. Z. Y. Fan, H. B. Zhu, H. T. Li, and J. Li, Magnon squeezing via reservoir-engineered opto-magnomechanics, *APL Photonics* 9(10), 100804 (2024)
12. Y. X. Luo, L. J. Cong, Z. G. Zheng, H. Y. Liu, Y. Ming, and R. C. Yang, Entanglement enhancement and EPR steering based on a PT-symmetric-like cavity-opto-magnomechanical hybrid system, *Opt. Express* 31(21), 34764 (2023)
13. K. Di, X. Wang, H. Xia, Y. Zhao, Y. Liu, A. Cheng, and J. Du, Macroscopic entanglement between ferrimagnetic magnons and atoms via crossed optical cavities, *Opt. Lett.* 49(11), 2878 (2024)
14. Y. Ashida, Z. Gong, and M. Ueda, Non-Hermitian physics, *Adv. Phys.* 69(3), 249 (2020)
15. R. El-Ganainy, K. G. Makris, M. Khajavikhan, Z. H. Musslimani, S. Rotter, and D. N. Christodoulides, Non-Hermitian physics and PT symmetry, *Nat. Phys.* 14(1), 11 (2018)
16. Y. W. Zheng, W. H. Xiao, X. Han, F. W. Hong, and S. Zhang, Nonreciprocal PT-symmetric magnon laser in spinning cavity optomagnonics, *Opt. Express* 32(4), 11 (2024)
17. F. Y. Zhang, Q. C. Wu, and C. P. Yang, Non-Hermitian shortcut to adiabaticity in Floquet cavity electromagnonics, *Phys. Rev. A* 106(1), 012609 (2022)
18. E. J. Bergholtz, J. C. Budich, and F. K. Kunst, Exceptional topology of non-Hermitian systems, *Rev. Mod. Phys.* 93(1), 015005 (2021)
19. L. Kong, M. H. Eldegail, and C. Xu, Extension of coherent perfect absorption-lasing effect and super-colli-

mation effect in an airborne phononic crystal with space-coiling structure, *Front. Phys.* 21(2), 024201 (2026)
20. Y. R. Zhang, Z. Z. Zhang, J. Q. Yuan, M. Kang, and J. Chen, High-order exceptional points in non-Hermitian moire lattices, *Front. Phys. (Beijing)* 14(5), 53603 (2019)
21. S. M. Hosseiny, H. R. Jahromi, B. Farajollahi, and M. Amniat-Talab, Technique for studying the coalescence of eigenstates and eigenvalues in non-Hermitian systems, *Front. Phys. (Beijing)* 20(1), 014201 (2025)
22. J. Chaste, A. Eichler, J. Moser, G. Ceballos, R. Rurali, and A. Bachtold, A nanomechanical mass sensor with yoctogram resolution, *Nat. Nanotechnol.* 7(5), 301 (2012)
23. B. B. Li, L. Ou, Y. Lei, and Y. C. Liu, Cavity optomechanical sensing, *Nanophotonics* 10(11), 2799 (2021)
24. X. Jiang, A. J. Qavi, S. H. Huang, and L. Yang, Whispering-gallery sensors, *Matter* 3(2), 371 (2020)
25. M. Li, H. X. Tang, and M. L. Roukes, Ultra-sensitive NEMS-based cantilevers for sensing, scanned probe and very high-frequency applications, Ultrasensitive nems-based cantilevers for sensing, scanned probe and very high-frequency applications, *Nat. Nanotechnol.* 2(2), 114 (2007)
26. W. Chen, Ş. K. Özdemir, G. Zhao, J. Wiersig, and L. Yang, Exceptional points enhance sensing in an optical microcavity, *Nature* 548(7666), 192 (2017)
27. Y. Wu, P. Zhou, T. Li, W. Wan, and Y. Zou, High-order exceptional point based optical sensor, *Opt. Express* 29(4), 6080 (2021)
28. J. Wiersig, Review of exceptional point-based sensors, *Photon. Res.* 8(9), 1457 (2020)
29. W. Mao, Z. Fu, Y. Li, F. Li, and L. Yang, Exceptional-point-enhanced phase sensing, *Sci. Adv.* 10(14), eadl5037 (2024)
30. P. Djorwe, Y. Pennec, and B. Djafari-Rouhani, Yan Pennec, and Bahram Djafari-Rouhani. Exceptional point enhances sensitivity of optomechanical mass sensors, *Phys. Rev. Appl.* 12(2), 024002 (2019)
31. X. Mao, G. Qin, H. Zhang, B. Wang, D. Long, G. Li, and G. Long, Enhanced sensing mechanism based on shifting an exceptional point, *Research* 6, 0260 (2023)
32. P. Djorwé, M. Asjad, Y. Pennec, D. Dutykh, and B. Djafari-Rouhani, Parametrically enhancing sensor sensitivity at an exceptional point, *Phys. Rev. Res.* 6(3), 033284 (2024)
33. Y. He and Q. Chen, Sensitivity of mass sensors enhanced by higher-order exceptional points in an optomechanical system, *Laser Phys.* 34(5), 055206 (2024)
34. H. Hodaei, A. U. Hassan, S. Wittek, H. Garcia-Gracia, R. El-Ganainy, D. N. Christodoulides, and M. Khajavikhan, Enhanced sensitivity at higher-order exceptional points, *Nature* 548(7666), 187 (2017)
35. C. Zeng, K. Zhu, Y. Sun, G. Li, Z. Guo, J. Jiang, Y. Li, H. Jiang, Y. Yang, and H. Chen, Ultra-sensitive passive wireless sensor exploiting high-order exceptional point for weakly coupling detection, *New J. Phys.* 23(6), 063008 (2021)
36. Z. Xie, Y. Wang, Z. Li, and T. Li, Enhanced rotation sensing with high-order exceptional points in a multi-mode coupled-ring gyroscope, *Opt. Lett.* 49(13), 3810 (2024)
37. Z. Lin, A. Pick, M. Lončar, and A. W. Rodriguez, Enhanced spontaneous emission at thir-dorder Dirac exceptional points in inverse-designed photonic crystals, *Phys. Rev. Lett.* 117(10), 107402 (2016)
38. K. Ding, G. Ma, M. Xiao, Z. Q. Zhang, and C. T. Chan, Emergence, coalescence, and topological properties of multiple exceptional points and their experimental realization, *Phys. Rev. X* 6(2), 021007 (2016)
39. I. Mandal and E. J. Bergholtz, Symmetry and higher-order exceptional points, *Phys. Rev. Lett.* 127(18), 186601 (2021)
40. G. Q. Zhang and J. Q. You, Higher-order exceptional point in a cavity magnonics system, *Phys. Rev. B* 99(5), 054404 (2019)
41. W. Xiong, Z. Li, Y. Song, J. Chen, G. Q. Zhang, and M. Wang, Higher-order exceptional point in a pseudo-Hermitian cavity optomechanical system, *Phys. Rev. A* 104(6), 063508 (2021)
42. L. Crippa, J. C. Budich, and G. Sangiovanni, Fourth-order exceptional points in correlated quantum many-body systems, *Phys. Rev. B* 104(12), L121109 (2021)
43. M. A. Miri and A. Alu, Exceptional points in optics and photonics, *Science* 363(6422), eaar7709 (2019)
44. H. Jing, Ş. K. Özdemir, H. Lü, and F. Nori, High-order exceptional points in optomechanics, *Sci. Rep.* 7, 3386 (2017)
45. C. Zeng, Y. Sun, G. Li, Y. Li, H. Jiang, Y. Yang, and H. Chen, Enhanced sensitivity at high-order exceptional points in a passive wireless sensing system, *Opt. Express* 27(20), 27562 (2019)
46. X. Zhang, C. L. Zou, L. Jiang, and H. X. Tang, Cavity magnomechanics, *Sci. Adv.* 2(3), e1501286 (2016)
47. S. Gröblacher, K. Hammerer, M. R. Vanner, and M. Aspelmeyer, Observation of strong coupling between a micromechanical resonator and an optical cavity field, *Nature* 460(7256), 724 (2009)
48. F. Heyroth, C. Hauser, P. Trempler, P. Geyer, F. Syrowatka, R. Dreyer, S. G. Ebbinghaus, G. Woltersdorf, and G. Schmidt, Monocrystalline freestanding three-dimensional yttrium-iron-garnet magnon nanoresonators, *Phys. Rev. Appl.* 12(5), 054031 (2019)
49. C. Jiang, Y. Cui, Z. Zhai, H. Yu, X. Li, and G. Chen, Tunable slow and fast light in parity-time-symmetric optomechanical systems with phonon pump, *Opt. Express* 26(22), 28834 (2018)
50. J. Li, S. Y. Zhu, and G. S. Agarwal, Magnon–photon–phonon entanglement in cavity magnomechanics, *Phys. Rev. Lett.* 121(20), 203601 (2018)
51. Z. Yang, B. Xiong, C. Zhao, and L. Zhou, Generation of multipartite entanglement in a cavity-magnomechanical system, *Opt. Express* 33(1), 5123 (2025)
52. C. Li, B. Xiong, Y. Wei, and C. Shan, Enhanced magnon blockade in a magnomechanical system, *Phys. Scr.* 99, 035118 (2024)
53. J. Cao, M. Wei, Q. Guo, H. Tan, G. Li, and T. Zhang, Generation and manipulation of one-way steering in optomagnomechanical system, *Adv. Quantum Technol.* 8(8), 2400547 (2025)
54. X. Zhang, C. Cao, Y. Gao, L. Fan, R. Zhang, and C.

Wang, Generation and manipulation of phonon lasering in a two-drive cavity magnomechanical system, *New J. Phys.* 25, 053039 (2023)
55. Q. Zhang, Y. Zhou, F. Liu, X. Wang, Y. Gao, L. Fan, and C. Cao, Magnon-squeezing-enhanced phonon lasering in cavity magnomechanics, *Adv. Quantum Technol.* 7(9), 2400200 (2024)
56. W. Chen, J. Zhang, B. Peng, Ş. K. Özdemir, X. Fan, and L. Yang, Parity-time symmetric whispering-gallery mode nanoparticle sensor, *Photon. Res.* 6(5), A23 (2018)
57. H. Loughlin and V. Sudhir, Exceptional point sensors offer no fundamental signal-to-noise ratio enhancement, *Phys. Rev. Lett.* 132(24), 243601 (2024)
58. M. Zhang, W. Sweeney, C. W. Hsu, L. Yang, A. D. Stone, and L. Jiang, Quantum noise theory of exceptional point amplifying sensors, *Phys. Rev. Lett.* 123(18), 180501 (2019)
59. X. Zheng and Y. D. Chong, Noise constraints for nonlinear exceptional point sensing, *Phys. Rev. Lett.* 134(13), 133801 (2025)
60. R. Kononchuk, J. Cai, F. Ellis, R. Thevamaran, and T. Kottos, Exceptional-point based accelerometers with enhanced signal-to-noise ratio, *Nature* 607(7920), 697 (2022)
61. A. Suntharalingam, L. Fernández-Alcázar, R. Kononchuk, and T. Kottos, Noise resilient exceptional-point voltmeters enabled by oscillation quenching phenomena, *Nat. Commun.* 14(1), 5515 (2023)
62. N. Wu, K. Cui, Q. Xu, X. Feng, F. Liu, W. Zhang, and Y. Huang, On-chip mechanical exceptional points based on an optomechanical zipper cavity, *Sci. Adv.* 9(3), eabp8892 (2023)
63. M. Khanbekyan, Exceptional-point-enhanced coupled microcavities for ultrasensitive particle sensing, *Phys. Rev. A* 108(2), 023710 (2023)
64. Z. Li, C. Li, Z. Xiong, G. Xu, Y. R. Wang, X. Tian, X. Yang, Z. Liu, Q. Zeng, R. Lin, Y. Li, J. K. W. Lee, J. S. Ho, and C. W. Qiu, Stochastic exceptional points for noise-assisted sensing, *Phys. Rev. Lett.* 130(22), 227201 (2023)